Metals and Materials International (2024) 30:2296–2315
https://doi.org/10.1007/s12540-024-01643-7

Texture Analyses and Mechanical Behavior of a High-Mn Steel Subjected to Different Pass Number of Simple Shear

Marcos Natan da Silva Lima[1,2,6] · Samuel Filgueiras Rodrigues[3] · Majid Al-Maharbi[4] · Laia Ortiz-Membrado[5] · Maria Veronica Goncalves Rodrigues[3] · Jessica Calvo Muñoz[6] · Emilio Jiménez-Piqué[5] · Gedeon Silva Reis[3] · José María Cabrera Marrero[6] · Hamilton Ferreira Gomes de Abreu[1,2]

Received: 30 October 2023 / Accepted: 29 January 2024 / Published online: 9 March 2024
© The Author(s) under exclusive licence to The Korean Institute of Metals and Materials 2024

Abstract
The microstructural evolution of TWIP steels under high strain-induced microstructural refinement is complex and requires careful investigation. A FeMnCrC TWIP steel was effectively deformed by simple shear through the equal channel angular pressing (ECAP) technique at 350 °C up to eight passes, using route Bc. Microstructure characterizations of the as-received and ECAP-processed specimens were performed by means of X-ray diffraction, Scanning Electron Microscopy and Electron Back-Scattered Diffraction. The High-speed nanoindentation technique has been used to analyze the mechanical properties. The correlation between microstructure, texture orientation, and grain refinement was systematically investigated. After the first pass, the sample presented A1*, A2*, and C as the most potent components. Samples that experienced the highest number of passes presented the highest intensity of fiber B. After the ECAP cycle, the investigated steel presented a homogeneous ultra-fine-grained structure. Nanoindentation maps suggested isotropic mechanical properties. The metal showed a significant increase in yield strength and high Ultimate tensile Strength compared to the as received. The high density of mechanical twinning, reduced grain size, and subgrains contributed to increased mechanical properties. Additionally, the severe plastic deformation increased the strength of the metal due to the gradual transition from homogeneous to heterogeneous microstructure composed of shear bands, dislocations, and micro-twin colonies. The results show that using the ECAP deformation technology can improve the mechanical properties of TWIP steels and reveal that the investigated metal has excellent potential to be employed in industry.

Keywords ECAP · High manganese TWIP steel · Mechanical properties · Microstructure · Texture

1 Introduction

The high-manganese austenitic steel (15–30 wt%) has garnered significant interest because of its remarkable blend of superior properties like, high strength, good ductility, low thermal expansion coefficient, suitable fatigue characteristics, formability and toughness in conjunction with the twinning-induced plasticity (TWIP) phenomenon [1–3]. Austenitic steel with high Mn content and low stacking fault energy (SFE), i.e., less than approximately 40 mJ/m^2, mechanical twinning occurs during plastic strain at low temperatures in face-centered cubic (FCC) structure. The mechanical twins serve as obstructions to sliding dislocations, causing a reduction in the effective mean free path of sliding dislocations within {111} slip planes [4]. Despite their exceptional properties, the use of these steels in modern equipment is restricted due to their comparatively low yield strength [5]. Enhancing the yield strength of this type of steel is currently a significant concern for its potential applications in the energy and petrochemical sectors. As a result, investigations into microstructure modification and grain refinement, have been initiated to augment the strength of these steels, which consequently influenced the texture [6, 7]. The SFE, which is regulated by temperature and chemical composition, plays a significant role in influencing the straining mechanisms of these steels, particularly mechanical twinning and dislocation slip. Through Hall–Petch effect, an increase in strength can be achieved due to strain, leading to the augmentation of dislocation density and the modification of dislocation structures via mechanical twinning [8, 9].

SPD technology, which employs the application of substantial shear stresses under high pressure, represents a

Extended author information available on the last page of the article

suitable approach to substantially enhance the grain refinement of metal alloys beyond the capabilities of conventional metal forming methods [10–15]. Few researchers have addressed the SPD of TWIP steels with high Mn content [16–20]. Abramova [16] employed high-pressure torsion (HPT) on multiple TWIP steels and observed substantial microstructure, hardness, and yield stress enhancements for all the samples. ECAP, another SPD method, can produce much larger nanostructured workpieces than other processes [21]. The initial investigations of TWIP steels treated with ECAP demonstrated that the microstructure underwent significant modifications following a single pass of the process [22]. Numerous researchers [19, 23, 24] have documented the presence of complicated microstructure that includes a combination of microband strain, subgrains, dislocation tangles and cells, nano- and micro-twins and stacking faults, in TWIP steels subjected to multiple passes of ECAP. In addition, the nucleation of nano-twins within micro-twins/microbands has been reported in previous studies [17]. Timokhina et al. [17] reported excellent mechanical properties, yield of 1480 MPa and tensile strength of 1624 MPa, in a TWIP steel. However, no more than four passes of ECAP are typically conducted on TWIP steels due to the difficulty in processing them using this method. There is a risk of specimen breakage, even after a single pass of ECAP [22].

While some researchers have proposed that the temperature at which the dominant deformation mode shifts from dislocation slip to twinning is approximately 300 °C, others have observed twinning activity even after ECAP treatment at temperatures as high as 400 °C [17, 19, 22]. According to a recent publication, the maximum values for yield stress and ultimate strength of TWIP steel processed by ECAP are 1480 MPa and 1675 MPa, respectively, and no higher values have been reported to date. It is important to note that when comparing the mechanical properties of TWIP steel displayed in the literature, the alloying elements must be considered since the chemical composition of high Mn content TWIP steel may vary significantly [17, 19, 25].

The TWIP steel chemical elements evaluated in this work are a key point. It is an aluminum-free steel with a high chromium content and the inclusion of copper. Adding aluminum and copper to the steel enhances its resistance to atmospheric corrosion, with the steel's resistance being three to five times greater than that of unalloyed ones [26]. Including copper slows down the rate at which twinning occurs and alters the pattern of sudden changes in stress and strain. Furthermore, introducing this element significantly boosts the total amount of deformation that can be achieved without any reduction in strength [26]. Limited studies have investigated the effects of SPD on high Mn and medium C steels and the TWIP effect. As far as known, there has been limited research on exploring the mechanical properties of the newly developed ECAP-treated TWIP steel studied in this work. Thus, the objective of this study is to assess the specific parameters regarding the pass number employed during SPD and to characterize the changes in microstructure using electron backscatter diffraction (EBSD), scanning electron microscopy (SEM), and texture, as well as the impact of the quantity of deformation on the resulting mechanical properties.

2 Material and Experimental Procedure

In this research, an austenitic high-Mn TWIP steel was examined as a potential replacement for conventional metals utilized in the petroleum sector, such as high-strength, low-alloy steels and pearlitic steels. A steel industrial company provided hot-rolled thick plates as the material for the investigation. In the course of metal production, the material went through hot rolling following continuous casting, and later, it underwent annealing in accordance with their industrial strategy. To determine the chemical composition, Optical Emission Spectroscopy (OES) was conducted using a Shimadzu Spectrometer, model PDA 7000. The resulting composition was 0.45 wt% carbon, 26.05 wt% manganese, 3.4 wt% chromium, 0.45 wt% copper, and the remaining balance being iron. The stacking fault energy (SFE) was calculated to be approximately 21 mJ/m^2 at room temperature and 69 mJ/m^2 at 350 °C, using the thermodynamic model presented in references [27, 28].

The supplied material was machined into cylindrical specimens with a diameter of 8 mm and a length of 55 mm, which were then subjected to the ECAP process. The ECAP technique involves cyclic pressing of the billet through a die-set that contains channels with the same periphery bisected at a specific angle. The process geometry involves simple shear, and the design of the equipment enables the application of high stresses on bulk materials of various materials, including steels and alloys [29]. The die utilized for the ECAP experiments was made of tool steel, and it comprised an insert die that consisted of two channels that intersected at an internal angle of 120° (refer to Fig. 1). The specimens underwent severe plastic deformation through route Bc [30], which involves rotating the specimen 90° along its longitudinal axis keeping the same direction during the strain passes [31]. The hydraulic press with a punch speed of 2 mm/s and a maximum capacity of 80 tons was utilized for the experiments. One, two, four, and a maximum quantity of 8 passes were performed over the metal at 350 °C. Iwahashi's relationship predicts that the internal angle of 120° promotes a true strain of approximately 0.6 after each pass [32]. A lubricant composed of both molybdenum disulfide (MoS_2) and graphite powder was used to decrease friction between the punch, die wall, and specimen during the experiments.

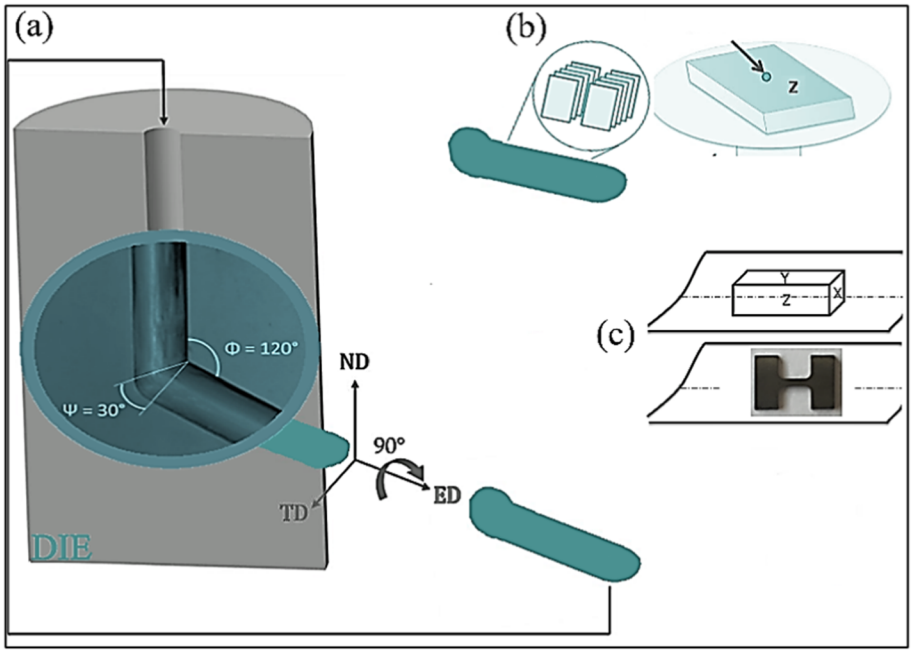

Fig. 1 (**a**) ECAP die configuration and Route Bc, along with the corresponding coordinate system utilized in this study, where ND represents the normal direction, ED represents the extrusion direction, and TD represents the transverse direction. (**b**) Chosen areas to examine the microstructure, microtexture, and the (**c**) micro-tensile specimens

The specimens underwent standard metallographic preparation methods, which included grinding using SiC papers of #400 to #1200 grits, followed by mechanical polishing with diamond paste of 6, 3, and 1 µm, and, ultimately, a 0.05 µm colloidal silica suspension. A (40% HNO3 + 60% H2O) solution was utilized for 3 s to perform chemical etching. The microstructural analyses of the original and deformed specimens were carried out through Optical Microscopy (OM) and Electron Microscopy on an FEI Quanta FEG 450 along the transverse plane.

X-ray diffraction (XRD) analysis was employed with the aim of identifying the phases in the material without and after the ECAP passes. It was used a Panalytical X'Pert Pro X-ray diffractometer equipped with a PW3121/00 Difracted Beam Flat Crystal Monochromator type for Co ($K\alpha_1 = 1.78897$ Å) radiation source, used at 40 kV and 40 mA with a monochromator. This analysis was performed with a scanning rate of 0.5°/min, and the range of analysis was from 45° to 120° [33]. The dislocation density was estimated using GND (Geometric Necessary Dislocations). The GND calculation used the method developed by Pantleon [34], implemented in the ATex toolbox (software) [35], and using EBSD data.

To prepare the EBSD samples, they were first ground with #400 to #2000 SiC papers and then subjected to electrolytic polishing using a solution containing 60% ethanol, 34% n-butanol, and 6% perchloric acid. The samples were polished at a voltage of 20 V and a current that varied from 0 to 2 A for 1 to 3 min, at 10 °C. EBSD measurements were obtained using FEI Quanta FEG 450 and JEOL JSM-7001F microscopes, which were operated at 20 kV. The working distance was adjusted to approximately 13 mm, while the sample was tilted at an angle of 70°. The orientation of the extrusion direction (ED), normal direction (ND), and transverse direction (TD) can be observed in Fig. 1. These directions correspond to the 'x', 'y', and 'z' axes, respectively. The annealed condition was scanned using a step size of 0.3 µm, while a step size of 0.1–0.05 µm was used for the sample with 2 ECAP passes. For the samples with 4 and 8 passes, a smaller step size of 0.03 µm was used. All captured grains of each image were used to represent the texture. The initial condition sample had an indexation rate of above 95%, while the samples maintained a rate of 80% or higher after the ECAP procedure. The data obtained from the EBSD scans were processed using the HKL Channel 5 software, where suitable noise reduction was employed. High-angle boundaries were defined as grain boundaries with a misorientation angle above 15°, while low-angle boundaries were identified as subgrain boundaries with a misorientation angle between 2° and 15°. A specific misorientation was selected for twin boundaries. Microtexture analysis was performed in the ATEX data processing software [35] in order to obtain texture images. The statistical Kernel density estimation method was utilized to determine the ODFs from EBSD maps.

Elastic modulus (E) and Hardness (H) indentation measurements were obtained by using an iNano®nanoindenter (KLA, Milpitas, CA, USA) equipped with a diamond, Berkovich tip. E and H related nanoindentation maps were built by using the called NanoBlitz high-speed mechanical property mapping technique. Each measurement was done in a very short time, which included the process of positioning

the tested region under the penetrator, approaching the surface, loading, unloading and lifting up the indenter. This technique provides mechanical mapping measured over a reasonable area (micrometric range) by making arrays of numbers of impressions, each consolidated by the method of Oliver and Pharr [36, 37]. Three maps of $200 \times 200 \mu m^2$ with 30,000 impressions (10,000 per specimen) were obtained using a load control of 5 mN, corresponding to a penetration depth of the indenter ranging from 170 to 200 nm. In order to avoid overlapping effect of neighboring prints, a spacing of 2 µm was used as well as the indentation depth/spacing ratio of 10 as suggested by Phani and Oliver [38]. The Poisson's ratio was set at 0.3, which is representative for steels and other metals [39]. Finally, the experimental maps were obtained, resulting in the average and standard deviation of E and H for the corresponding amount of applied strain. The high-speed nanoindentation mappings present E and H measurements for individual phases and orientations, showcasing distinct micro length-scale mechanical properties. However, for comparative purposes, average values for these properties were reported.

As shown in Fig. 1, the micro-tensile samples were machined from the center of the longitudinal section of the ECAP-processed specimens. A micro-test machine was utilized to perform tensile testing under quasi-static loading conditions, with a cross-head speed of 3.3×10^{-3} mm/s. The tests were conducted using a micro test (DEBEN) machine. The engineering stress–strain curves were converted into stress/logarithmic strain curves using the relations $\sigma_t = \sigma_{eng}\left(\varepsilon_{eng} + 1\right)$ and $\varepsilon_t = ln\left(\varepsilon_{eng} + 1\right)$. Mechanical properties, like yield, ultimate strength, and elongation, were captured directly from the stress–strain curves. The area under the elastic regime was used to calculate the resilience, while the whole region under the flow curse was used to determine the toughness. The SEM with a field emission gun JEOL JSM-7001F was used to examine the fracture surfaces at a voltage of 20 kV. High-resolution fracture images were obtained and analyzed.

3 Results and Discussion

3.1 Characterization of Microstructure and Hardness

The micrographs were taken at the cross sections, i.e., normal direction parallel to the 'z' axis, for all samples, i.e., initial sample and after 1, 2, 4 and 8 ECAP passes. The microstructure of Fig. 2a displays a refined austenite phase consisting mainly of equiaxed grains. The microstructure also exhibits the presence of thermal twins as result of the hot-rolling process, along with a few mechanical twins that arose during sample preparation. The observation reported in an earlier publication [33, 40, 41] agrees with the microstructure of the as-received sample. The microstructure of the samples after 1, 2, 4, and 8 ECAP passes are presented in Fig. 2b–e, respectively. Mechanical twins (white arrow) can be seen as a consequence of the applied passes. Upon subjecting to first ECAP pass, the grains were observed to elongate parallel to the shear direction. Figure 2b shows the presence of plastically deformed and longitudinally elongated grains. The occurrence of mechanical twins is related

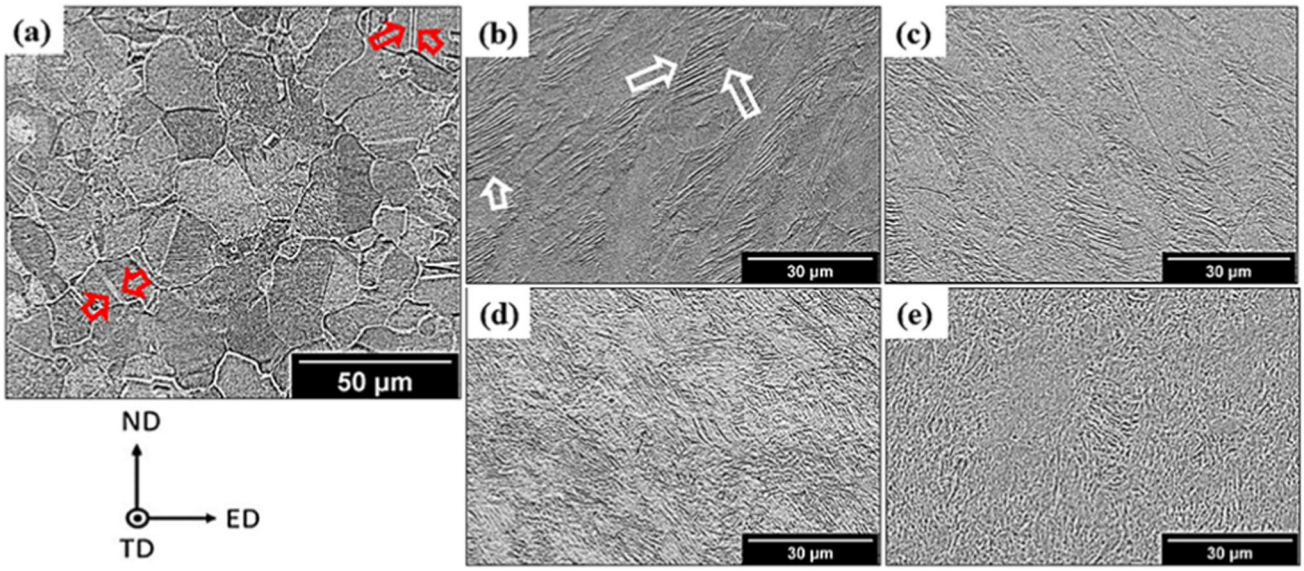

Fig. 2 FEG-SEM secondary electron micrographs of samples, showing the microstructure evolution from (**a**) as-received, (**b**) after 1, (**c**) after 2, (**d**) after 4, and (**e**) after 8 ECAP passes. Mechanical twins are highlighted with white arrows, while annealing twins are marked in red

to a low value of Stacking Fault Energy (SFE). Even though the SFE of the material increased due to the deformation temperature at 350 °C, appropriately oriented grains showed high deformation twin bundles reactions, as shown in the inset of Fig. 2. Annealing and deformation twins, bands and micro shear bands at the grain scale were identified as the longitudinal deformation features. Plastic deformation of the grains at the same direction of shear was observed with continuous shearing in the planes after the rotation of the sample between each pass for two, four, and eight passes, as shown in Fig. 2c–e. This analysis agrees with another research published elsewhere [25, 26]. Mechanically induced twinning was observed to occur on deformation micro shear bands in samples that underwent 8 ECAP passes. The austenite grains exhibited a heterogeneous morphology structure, which can be attributed to the formation of micro shear bands during the application of the shear. The formation of micro shear bands, which results from the shear process, gradually develops as the number of ECAP passes increases. This structure is characterized by a heterogeneous morphology, including ultrafine grains and dislocation tangles, as previously reported by Wang et al. [19, 24].

3.2 X-Ray Diffraction Characterization

Figure 3 illustrates the XRD patterns of all the analyzed samples. The as-received sample exhibited a sole austenitic phase. The XRD analysis of the ECAP specimens revealed that no other phases, including α′ and ε martensite, were present. The high Mn content (26.05 wt%) acts as an austenite stabilizer, resulting in the observation of only the TWIP effect. In the ECAP-deformed samples, it was noticed that the diffraction peaks were displaced towards the left in the quantity of one degree (±51° from to 50°), accompanied by an increase in peak width. The literature has reported that deformation-induced lattice distortion can shift the diffraction angles' peak position [42]. Broadening of the diffraction peaks can be caused by dislocations. The peak shift, coupled with the broadening, indicates that there has been an increase in dislocation density and lattice distortion, which are caused by plastic deformation. The asymmetry in diffraction peaks is another result of lattice distortion and indicates Coincidence Site Lattice (CSL) boundary formation [43].

The ECAP process leads to a high dislocation density, which creates a localized distortion of the lattice structure,

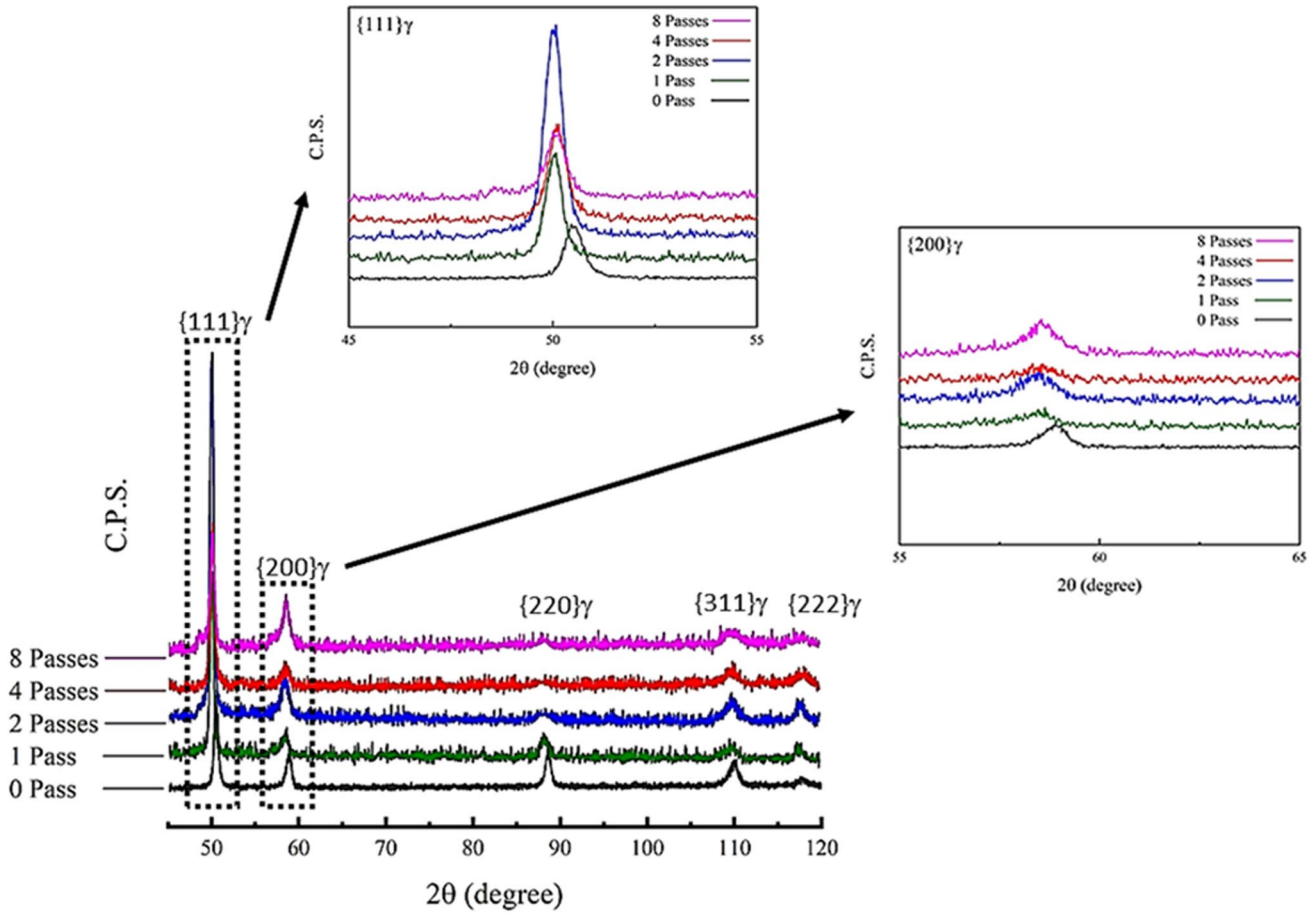

Fig. 3 XRD patterns of the encountered plans of all samples. Planes {111} and {200} are highlighted

resulting in a modification of the peak shape observed in diffracted patterns. The magnitude of peak broadening can provide an indirect indication of changes in dislocation density in metallic materials [43]. The results showed that the dislocation density was 2.23×10^{13} m^{-2} for the as-received specimen and increased to 8×10^{15} m^{-2} after 8 ECAP passes. Figure 4 illustrates the dislocation density increase of all samples. The dislocation density maps of the as received and after 8 ECAP passes are also shown in Fig. 4. Materials with low SFE usually exhibit a mechanism that generates partial dislocations instead of screw dislocations [44, 45]. Screw dislocations that cannot undergo cross-slip result in limited dislocation motion. Therefore, the density of dislocations significantly increases due to pile-up and proliferation of dislocations. After the pass number 2, a noticeable increase in the dislocation density is observed. Furthermore, considerable refinement was observed in the microstructures shown in Fig. 2 and later in Fig. 6, indicating a significant increment in dislocation density. The microstructure also undergoes further refinement after four and eight passes, although at a sluggish rate, owing to the substantial strain already imposed on the metal. As a result, the determined dislocation density exhibits a lower increase, indicating a deceleration in the formation of the dislocation rate. The ECAP process results in an increased dislocation density that induces higher distortion of the crystal lattice, leading to an increase in the stored energy of the material. Consequently, the material exhibited elongated grains, twin contours and the formation of shear bands, consistent with the previously reported hardness results [43].

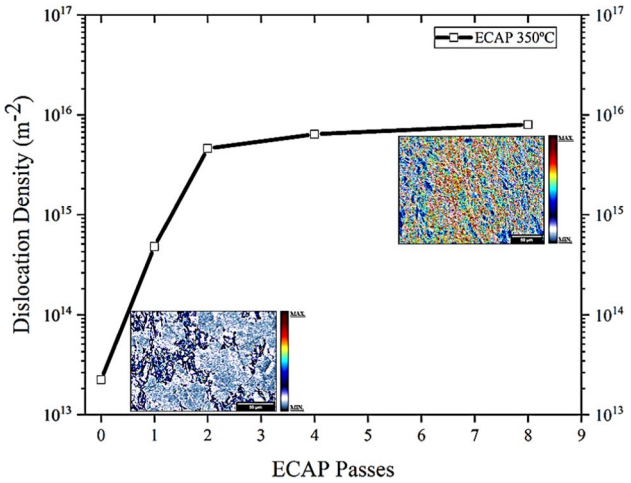

Fig. 4 Representation of the dislocation density on ECAP pass number. dislocation density of the as received and after 8 passes is shown

3.3 Electron Backscatter Diffraction (EBSD) and Texture Characterization

Figures 5 and 6 display the orientation image maps (OIMs) and grain boundary maps of initial and those samples after ECAP deformation, which were acquired by using the EBSD. The Figures showed that there was a gradient in texture inside the grains with increasing deformation. Based on Fig. 5, it can be observed that the material possesses a relatively uniform microstructure that consists of equiaxed grains having an average size of 7 μm ± 1 μm (excluding twins). The green lines in the microstructure maps indicate the presence of twins, while the black lines represent the high-angle grain boundaries. Subgrains were not observed in this condition. Figure 5 also includes an Inverse Pole Figure (IPF) map and Orientation Distribution Functions (ODFs) at $\varphi_2 = 0°$ and $\varphi_2 = 45°$ sections in the Euler space of the investigated samples. The as-received sample exhibited preferred crystallographic orientations along (001)[100] and (001)[120]. The appearance of the (001)[100] cleavage cube component in the initial sample could be a consequence to the formation of columnar grains during solidification, that were refined along the maximum heat conduction direction and with dynamic recrystallization, as reported in previous studies [46]. Zhang et al. [47] found that the {001} < 120 > components, are mainly formed during the recrystallization of {001} columnar grains, result in low corrosion and mechanical resistance. The ODFs for the as-received samples were plotted using orthorhombic symmetry. These results agree with the values reported in the literature [41].

Figure 6 showcases the key characteristics of the microstructure following 1, 2, 4, and 8 passes, while Fig. 7 displays the progression profile of the mean grain size. After undergoing ECAP passes, elongated grains in the shear direction are observed, and in some regions, thin equiaxed grains can be seen. During the first pass, a significant number of low-angle grain boundaries were generated along with elongated grains in the shear direction (Fig. 6b). Mechanical twins were also observed in certain regions (Fig. 6a). Although the grain size distribution is not homogeneous, the average grain size of the newly formed grains after one ECAP pass is 1 μm ± 0.6 μm. After 2 ECAP passes, the average grain size further decreases. The microstructure remains heterogeneous; however, the number of newly refined grains increases. As the number of ECAP passes increases, the presence of large and elongated grains in the microstructure gradually disappears and is replaced by a more refined structure, as shown in Fig. 6c, d. The microstructure of the metal subjected to 4 ECAP passes (Fig. 6e, f) shows deformation bands containing fine twins (shown in white) and progressive microstructure refinement.

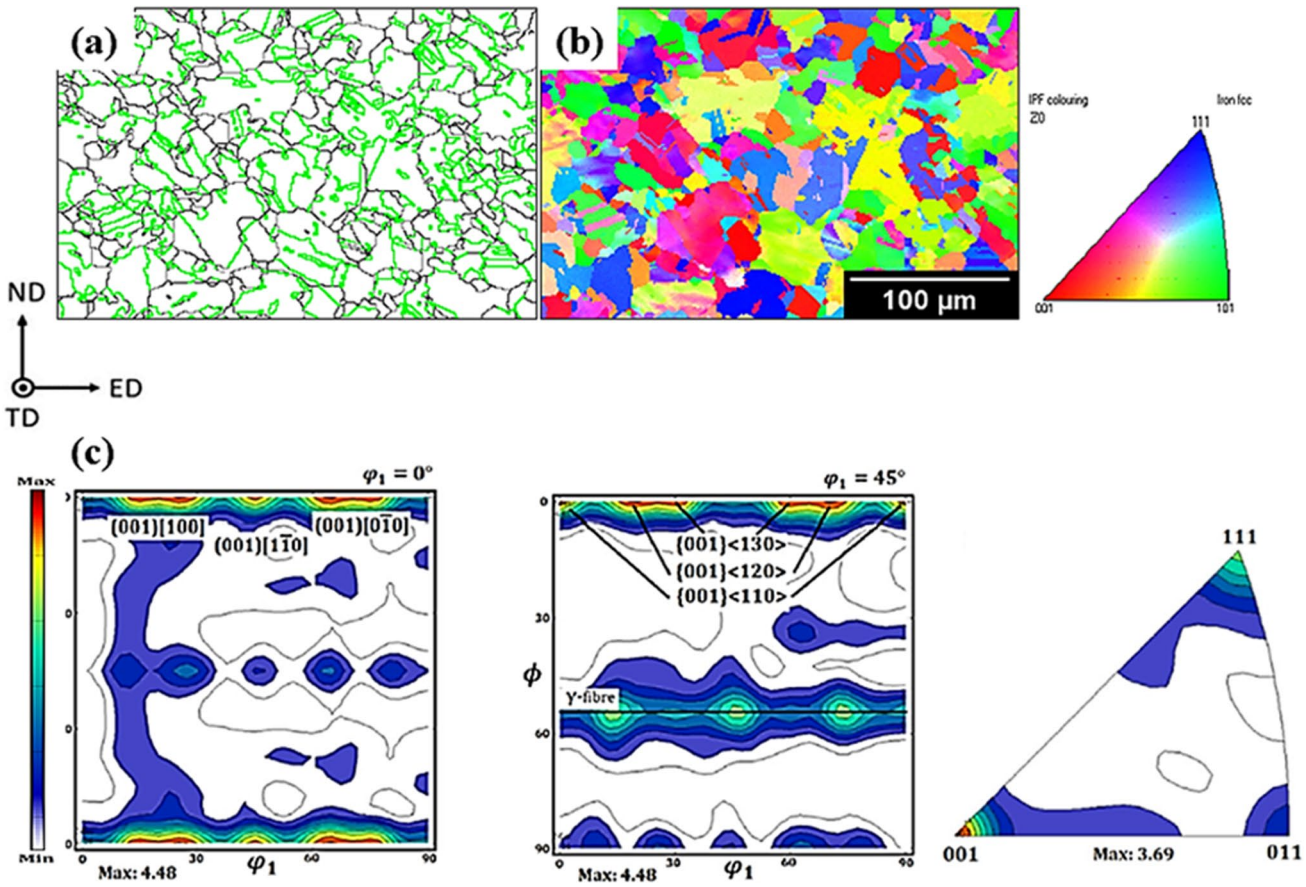

Fig. 5 EBSD grain map, grain boundary of the as-received sample, ((**a**) IQ mapping), (**b**) IPF mapping) (grains boundary map: black line—high-angle grain boundary, green line—twins boundary), corresponding (**c**) Inverse Pole Figure map and Orientation Distribution Function at constant $\varphi_2 = 0°$ and (d)$\varphi_2 = 45°$ sections of as-received sample

The microstructure refinement observed in the TWIP steel is achieved by intersecting various families of deformation bands, resulting in misaligned and disoriented structures [23]. Finally, after eight passes, the microstructure undergoes new qualitative changes, as the deformation bands transform into subgrains. The microstructure has undergone significant refinement, making it difficult to identify areas with a high concentration of defects, particularly subgrain boundaries (depicted in green). In some regions of the sample, there is a noticeable shift towards equiaxed grains, as shown in Fig. 6f, g. After eight passes, the average grain size was measured to be 0.20 µm ± 0.05 µm. Figure 7 illustrates how the average grain size (with misorientation > 15°) changes as a function of the number of ECAP passes. Still, no regular grain size of 0.20 µm after eight passes is observed. This behavior indicates the formation of a partially stable microstructure with an increasing number of passes. According to Fig. 6, the distributions after the fourth and eighth passes are similar, indicating that a steady state has not been reached even after eight passes [48].

The examined fragments exhibit a complex hierarchical defect structure, with numerous defects and twinned colonies subdividing the material into small sections. The deformation is concentrated in the deformation zone, which is formed by the intersection of the channels. After a few initial passes of ECAP, heterogeneity in the macroscopic strain distribution along the height of the processed parts can be observed, which is dependent on the geometry of the ECAP array. However, this macroscopic heterogeneity gradually diminishes with an increase in the number of passes. In the case of a round specimen cross-section [23, 31], these tendencies are less noticeable. Deformation twinning is observed throughout all stages of deformation during ECAP. However, it is important to consider the step sizes used in EBSD analysis and the lowest indexation rate in the most highly deformed samples. Accordingly, this technique is unsuitable for calculating the fraction of twins accurately, and also, many fine twins mechanisms need to be visible. The observed microstructural evolution of the TWIP steel during multi-pass ECAP at 350°C for up to four passes is

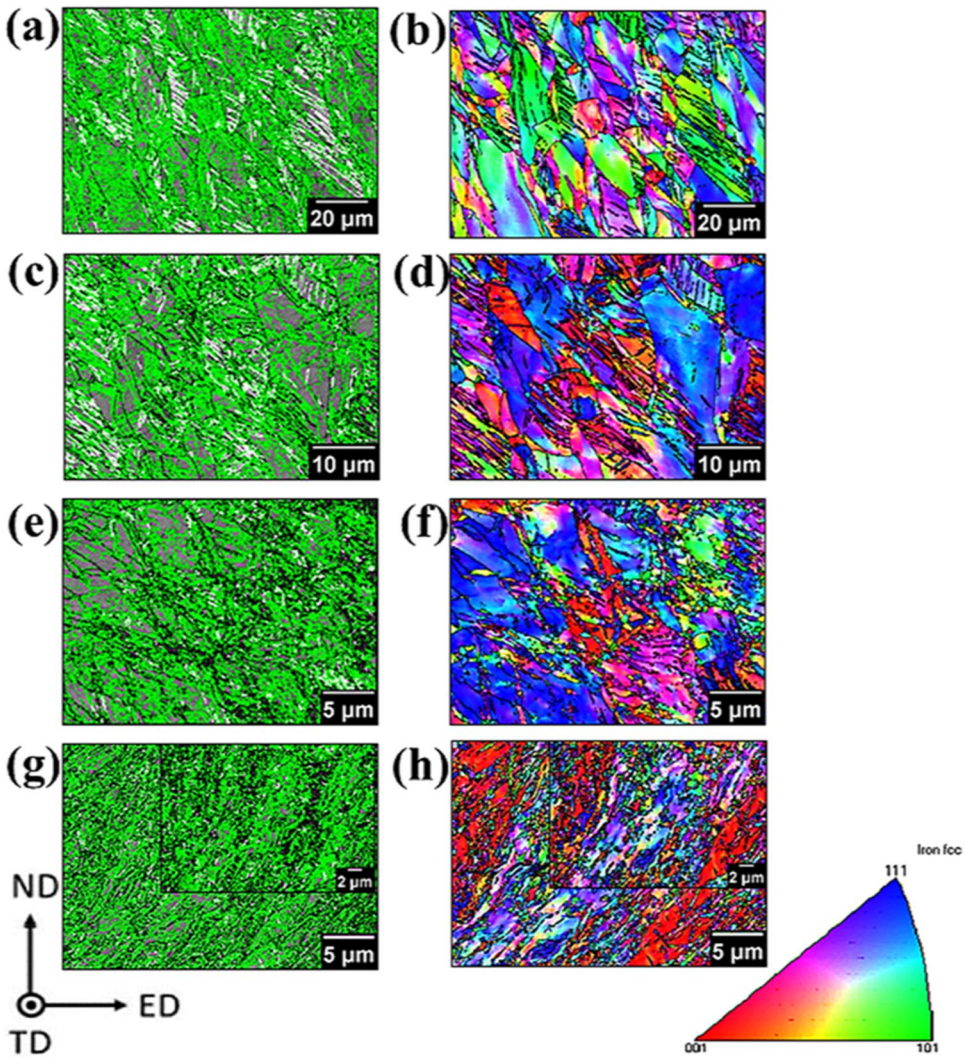

Fig. 6 EBSD features of the TWIP steel samples subjected to different numbers of ECAP passes at 350 °C. IQ mapping, grain boundary maps, and IPF. Images (**a**) and (**b**) show the features of the first pass, (**c**) and (**d**) represent the second pass. (**e**) and (**f**) display observations after the fourth pass, and (**g**) and (**h**) represent the eighth pass. In each image, the black lines correspond to high-angle grain boundaries, the green lines to low-angle grain boundaries, and the white lines to twin boundaries

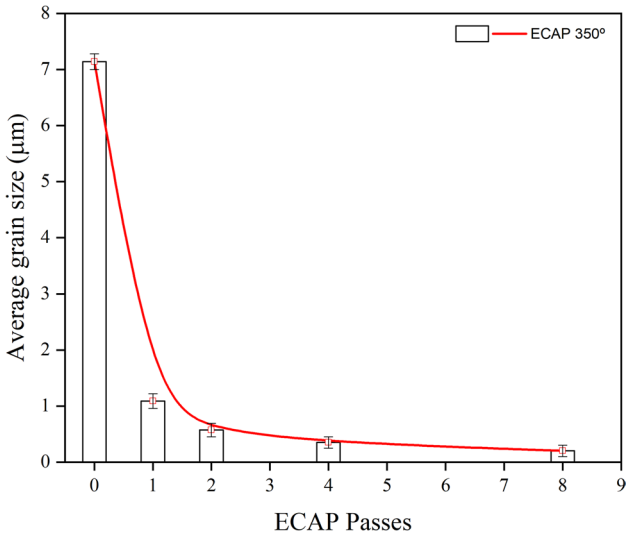

Fig. 7 Average grain size changes as a function of the number of ECAP passes

consistent with the previously published data on processing the material using similar dies and temperatures [19, 22–24].

The grain boundaries' characteristics (refer to Fig. 8) can determine the proportion of low angle grain boundaries (LAGBs, with an inclination angle of $2° < \Theta < 5°$), high angle grain boundaries (HAGBs, with an inclination angle of $15° < \Theta$), and coincidence site lattice (CSL) boundaries. New grains nucleate primarily in the shear bands and grain boundaries and due to the dislocation rearrangement. Dislocation tangles combine to form subgrains, eventually resulting in new grain boundaries [49]. A dynamic recrystallization process seems to have initiated in the microstructure after 4 ECAP passes, as shown in Fig. 8.

Upon analyzing the as-received sample, it was discovered that it exhibited the lowest proportion of low-angle misorientations due to dynamic recrystallization and recovery that occurred during the production of the steel. The original material has around 30% of the overall coincidence site lattice (CSL) boundaries. One can observe the generation

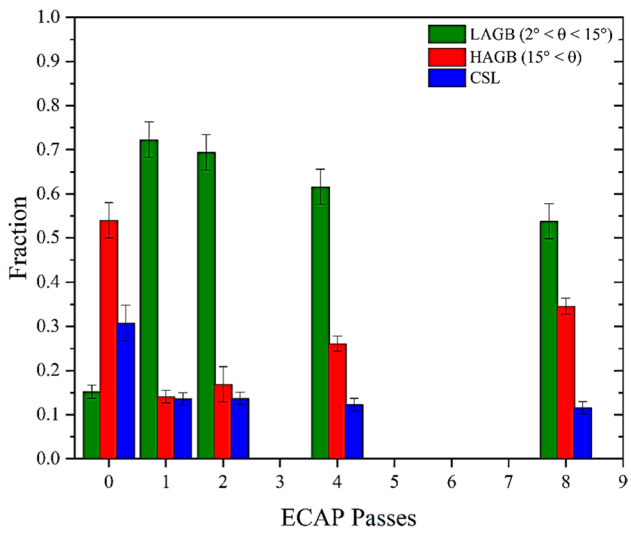

Fig. 8 Evolution of misorientation of the grain boundaries as the number of ECAP passes increases

of numerous subgrains in the first pass after ECAP, which gradually decreases with each subsequent pass (as depicted in Fig. 8). However, the introduction of deformation into the material after the second pass promotes an increase in the fraction of high angle grain boundaries (HAGBs), which, since the fourth pass, can be partially attributed to certain misorientation fractions that have a twin character with coincidence site lattice (CSL) boundaries. The distribution functions of misorientation were comparable between the fourth and eighth passes. However, there was a slight continuous increase in the fraction of HAGBs (from 22 to 35%) and a consequent decrease in the fraction of low misorientation grains (from 65 to 55%) from the fourth to the eighth pass, as observed in the misorientation distribution functions, Fig. 8. During ECAP passes, a significant number of dislocations and crystallographic defects are produced, leading to the formation of dislocation cell boundaries, and the development of deformation-induced boundaries with an increase in the number of passes [50].

The findings demonstrated that the gradual rise in grain misorientation with the progression of ECAP passes resulted in the fragmentation of grains and reorientation of texture components. Austenitic steels frequently exhibit the emergence of low-energy CSL boundaries, which involve twinning boundaries with $\sum 3, 9, 27^{n}$ misorientations [48]. The results of this study also indicate that the majority of CSLs are a result of the formation of slip bands and deformation twins. Yang et al. [25] proposed that deformation-induced twinning is also related to planar slip bands. The authors proposed that the planar-slip dislocations contain numerous Shockley partial dislocations that can significantly contribute to the formation of deformation twins. It is worth noting that as the amount of deformation increases, the fraction of CSL boundaries decreases, as shown in Fig. 8. However, it should be noted that this observation may be limited by the capabilities of the EBSD technique.

Crystallographic anisotropy is an important factor in the evolution of lattice distortion, which includes misorientation, and it is essential to analyze it at the level of individual grains. However, this aspect is beyond the scope of this study. The HAGB and LAGB fractions obtained in this study are higher than those proposed by Wang et al. [19, 24] in TWIP steel processed by ECAP via the Bc route. Nevertheless, it is important to note that several other studies [19, 22–24, 48] have reported the occurrence of saturation in the proportions of HAGB and LAGB with an increase in the ECAP passes number.

The texture evolution of the TWIP steel under ECAP processing was analyzed in the triclinic symmetry (0° < < 360°) following Beyerlein's suggestions [51] which is the ideal orientation of deformation by simple shear. Figure 9 illustrates how the texture changes in the material after one, two, four, and eight ECAP passes, and Table 1 shows the ideal orientation for texture components in FCC materials subjected to simple shear. The intensities of the $B/\overline{B}$ and $A/\overline{A}$ texture components are nearly identical. In some cases, monoclinic symmetry may be observed since the components exhibit symmetry every 180°. However, it should be noted that no monoclinic symmetry was observed following the Bc route after two and four ECAP passes, as reported by Beyerlein [51]. Monoclinic symmetry was observed in another research [52] that used a die with a configuration like the one used in this work.

The texture patterns exhibit prevailing orientations with continuous distributions along the fibers. This texture is referred to as a simple shear texture and occurs when the die possesses an external angle of Ψ greater than 0°, which creates two symmetrical areas [52]. Figure 9b shows the texture after 1 ECAP pass; all texture components related to shear, which are listed in Table 1, were rapidly generated and established a complete fiber at the coordinates of (0–360°, 45°, 0°), showing ideal components of the simple shear model as presented in Fig. 9a, with a few variations. It is common to observe variations in Euler space from ideal orientations during ECAP processes, which can be attributed to various processing factors [22, 51]. The presence of this effect was observed in all the conditions following the ECAP process. The TWIP steel shows the presence of A1* and A2* components, which are part of the α fiber, after one ECAP pass. This occurrence is indicative of twinning, which is in agreement with the images presented in Figs. 5 and 6. Other investigators have reported similar intensity values for the components in FeMnCAl TWIP steel, as described in previous studies [19, 22, 24]. The tendency for low-SFE metals to develop the B fiber orientations with increasing strain has been previously observed. The strengthening of component

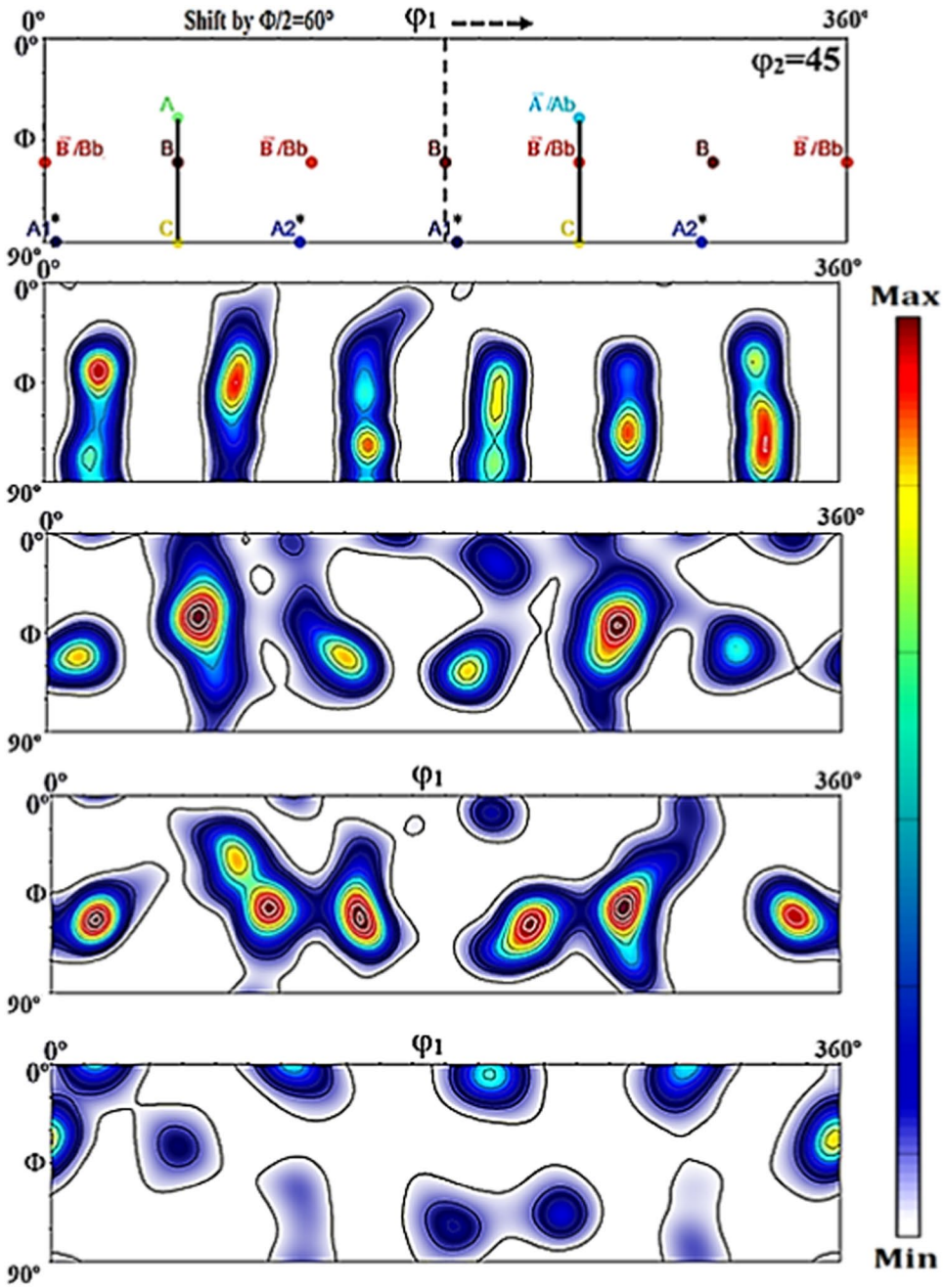

Fig. 9 (**a**) Theoretical components of FCC materials in triclinic symmetry deformed through simple shear (die 120°), texture constituents of the analyzed TWIP steel for φ2 = 45°, (**b**) post one ECAP pass, (**c**) post two ECAP passes, (**d**) post four ECAP passes, and (**e**) post eight ECAP passes

B has been observed to be related to the increase of fiber B, which is mainly a consequence of replacement of orientations of component C by B orientations ({112} < 110 >) [40]. These are consistent with the results of the present study.

As the SFE decreases, the texture component tends to change from C to A1*, and finally to B [53]. Similarities in the effect of SFE on texture evolution during ECAP and texture development during cold rolling have been suggested by other researchers [54]. The following correspondence was proposed: S = > A1*, Cu = > C, Brass = > $B/\overline{B}$. The texture components {112} < 111 > Cu and {123} < 634 > S are observed to decrease with decreasing SFE in the cold rolling texture, while the texture component {110} < 112 > Brass is observed to increase. As the SFE decreases, it is expected that the texture component C will decrease, while the texture components $B/\overline{B}$ will become stronger. After undergoing 4 ECAP passes, the TWIP steel being studied showed a decrease in the strength of the C texture component. Other low-SFE studied materials [22, 55] did not report a significant decrease in A2* and A1* components. However, the decrease in A2* and A1* intensities was observed in a FeMnCAl TWIP steel [19, 22, 24]. It is possible that the reduction in the intensities of A2* and A1* components is

Table 1 Ideal texture components for the ECAP die with a 120° angle [51]

Crystal structure	Texture components	φ1(°)	Φ(°)	φ2 (°)
FCC	A_1*	95.26/275.26	45	0
		5.26/185.26	90	45
	A_2*	24.74/204.74	45	0
		114.74/294.74	90	45
	A	60	36.26	45
	$\overline{A}$	240	35.26	45
	B	60/180/300	54.74	45
	$\overline{B}$	120/240/360	54.74	45
	C	150/330	45	0
		60/240	90	45
	{111}-/A-fiber	{111}<uvw>		
	<111>-/B-fiber	{hkl}<110>		

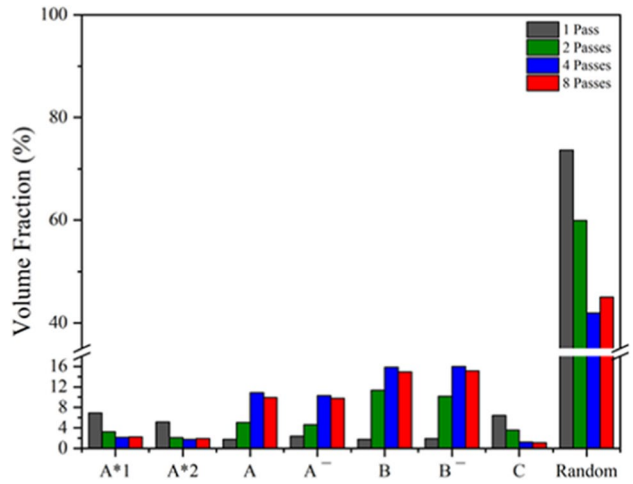

Fig. 10 Changes in the volume fractions of the primary texture components throughout the ECAP procedure

due to the limitations of EBSD analysis to detect all newly formed twins at high deformations, as reported in previous studies [19, 24].

Previous studies have reported an increase in the $B/\overline{B}$ components as low-SFE metals are subjected to higher levels of strain [51]. The intensity increase of the $B/\overline{B}$ components with increasing strain in low-SFE metals has been attributed to the replacement of C component orientations by $B/\overline{B}$ orientations ({112}[110]) [51, 52]. The evolution of the current texture is partially consistent with this line of reasoning, as there was indeed a decrease in the C component after four ECAP passes.

The texture of the material after two ECAP passes (Fig. 9c) exhibited some changes compared to the texture after one pass, including a reduction in the A1*, A2*, and C texture components and an increase in the $A/\overline{A}$ and $B/\overline{B}$ components. Previous studies have reported that embrittlement or saturation can occur between 2 and 4 ECAP passes using route Bc altering in this way the texture [56–59]. Additionally, the increase in the intensity of texture has also been observed in other study [55]. The texture was amplified, as demonstrated by a rise in the texture index and a reduction in the proportion of grains with random orientations, after four ECAP passes, according to Fig. 9d. It is noteworthy that, for steels similar to the one studied, the $B/\overline{B}$ and $A/\overline{A}$ texture components are characterized as a strengthening texture, while the A2*, A1*, and C components are weakened. After 8 ECAP passes (Fig. 9e), a mixed microstructure can be seen. Texture after 4 ECAP passes should generally remain the same. However, in the present work, the intensity in C and the appearance of texture components of recrystallization RB, Cb, Goss, and Brass appeared to increase, besides the observation of high intensity of the component $B/\overline{B}$. Figure 10 displays the progression of these volume fractions. According to Haase et al. [22], this texture observed in FeMnCAl can be considered a "transition texture". They hypothesized that the strong presence of component C in the texture could be attributed to dislocation sliding being the primary deformation mechanism. Simultaneously, the intensification related to the $B/\overline{B}$ components could be linked to the twinning mechanism. They also reported that the C component was strongly present and the $B/\overline{B}$ components increased with the number of ECAP passes. The texture evolution of FeMnCCr steel used in this study shows a better agreement with the correspondence proposed by Suwas et al. [60] and Wang et al. [19, 24], as the C and A1* components decrease, and the $B/\overline{B}$ component increases after ECAP passes. It can be inferred that the relevance of twinning deformation would be more pronounced in both scenarios.

Upon analyzing the anisotropy of the TWIP steel after the ECAP process (Fig. 11), it was observed that there was a preference for the fiber <110> ‖ × (direction of extrusion), which resulted in the presence of deformation texture components such as C, $B/\overline{B}$, and $A/\overline{A}$. These are texture components characteristic of a material subjected to simple shear. However, there is also a marked influence of the fibers <110> ‖ Z and <111> ‖ Y. Furthermore, the parallel direction to the Z axis presented a preference for the direction <110>, which could be associated with the highest amount of grain boundaries oriented in this direction. Figure 11 implies non-uniformity in the texture induced by the ECAP procedure, particularly when utilizing ECAP dies having Ψ > 0°. The presence of recrystallization texture components such as Cube, Goss, Brass, Copper, Brass rotated, and twinned Cube is suggested by the fibers <111> and <100>. The occurrence of the dominant fiber <111> ‖ Y may also be attributed to the existence of specific grain boundaries, such as the Σ3 (60° <111>) type.

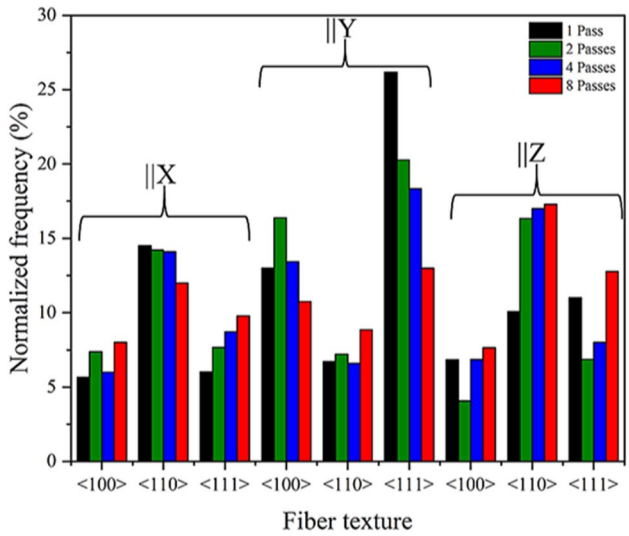

Fig. 11 Fiber texture of all samples after the ECAP process

In summary, the results showed that the investigated material initially deforms along the direction of the highest atomic density, which in FCC materials is the < 110 > direction or β fiber, characterized by the texture components C, $B/\overline{B}$, and A/Ā [48, 61].

As the level of deformation is increased, the formation of subgrains becomes more prominent and hinders the motion of dislocations. The grain orientation of the deformed TWIP steel samples exhibited progressive changes. These changes in grain orientation can be quantified using various indicators such as GAM, GOS, and KAM. GAM stands for the average grain misorientation, GOS measures the spread in grain orientation, and KAM stands for kernel average misorientation. As the amount of strain increased, the GOS distribution exhibited a peak shift towards a higher angle, indicating a higher dislocation density and more prominent substructures in the deformed samples. An increased upper limit of GOS with a broad distribution indicates a higher density of dislocations and a heterogeneous structure of dislocations. The observed changes in grain orientation and substructure, as well as the shift in GOS distribution, strongly indicate that at higher strain, slip activity increases at the expense of twinning in TWIP steel [62]. The Grain Orientation Spread (GOS) analysis involves calculating the mean variation in orientation between individual points within a grain and the overall average orientation of the grains. This method results in attributing an identical value to each scanning point present within the grain [63]. The examination of strain distribution within the crystal grains involved studying the local alterations in orientation among five adjacent pixels. For a grain to be recognized as valid, it needs to encompass a specified minimum quantity of scanning points. This predetermined size could also impact the results. By increasing the minimum grain size for the analysis, its necessary to exclude smaller grains or subgrains from the computations. Additionally, grains possessing orientation spreads of less than 2° were omitted from the analysis. With the enlargement of the minimum grain size, there is a consequent exclusion of minor subgrains located within the larger deformed grains. Inside a subgrain, the localized fluctuations in orientation could be notably minimal. Hence, with the augmentation of the minimum grain size, the trends tend to lean toward a greater proportion of grains exhibiting substantial orientation spreads [63]. Figure 12f shows the GOS results obtained from this analysis. The as-received sample showed the highest percentage of low GOS values (GOS < 1°), as depicted in Fig. 12a. Furthermore, this specimen displayed recrystallized austenite grains and exhibited minimal intergranular misorientation within its microstructure. After undergoing the ECAP process, a considerable number of grains in the TWIP steel showed medium (1° < GOS < 3°) and high (GOS > 3°) levels of misorientation, as illustrated in Fig. 12d, e. High values of GOS, as observed in Fig. 12b, c, may be related to significant local lattice distortion and dislocation density, which results in an increase in internal energy [64]. Throughout plastic deformation, various crystallographic defects like dislocations, shear bands, and grain boundaries emerged. These defects were later assimilated and joined to create dislocation cells, low-angle boundaries, and nano-twins. The concentrated stored strain energy caused by lattice misalignment functions as an obstacle to dislocation movement, potentially resulting in reduced toughness and heightened mechanical strength. The reduction of GOS values suggests the beginning of dynamic recrystallization with subgrains developed during plastic deformation at 350 °C.

3.4 High-Speed Nanoindentation Mapping

A SEM image of a selected area corresponding the region where the property maps (H, E and H/E ratio) were obtained after the prints are shown in Fig. 13. Nanohardness and modulus of elasticity maps obtained after the high-speed nanoindentation tests are shown in Figs. 14. Quantification can be seen in Table 2. Mechanically distinct regions can be perfectly distinguished (Fig. 14). The hardness after ECAP occurred more intensively in an isotropic manner (Fig. 14d1–e3), and the average nanohardness values increased significantly, indicating the strengthening of the material (Table 2). In the samples that passed through the highest number of ECAP passes, a homogeneity trend occurred (Fig. 14). The initial objective of identifying zones with a higher number of twins was achieved up to the samples with 2 ECAP passes. For samples with a higher number of passes and consequently higher deformation, it became difficult to separate regions

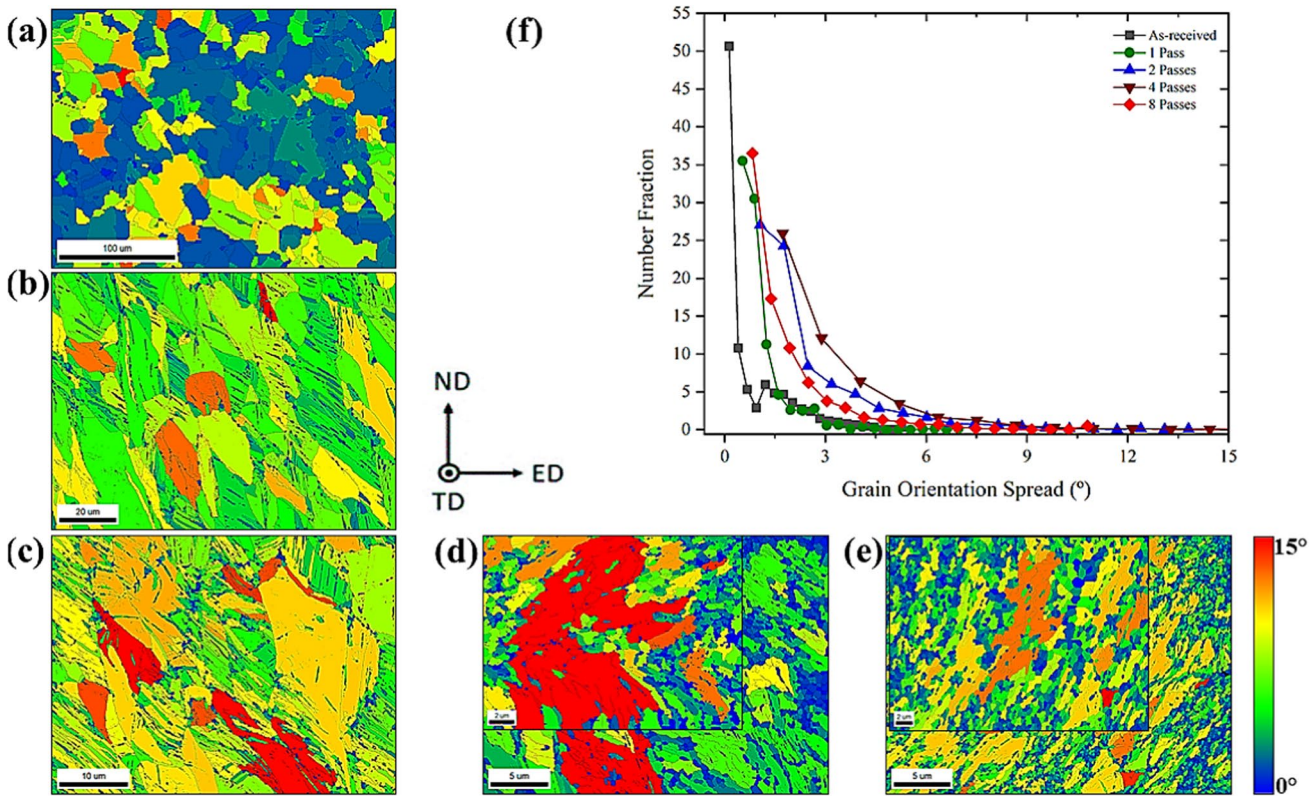

Fig. 12 GOS maps obtained from EBSD analysis of the investigated specimens, including the as-received sample (**a**) and samples after different numbers of ECAP passes (**b**–**e**). The variation of GOS distribution for all specimens is also presented (**f**)

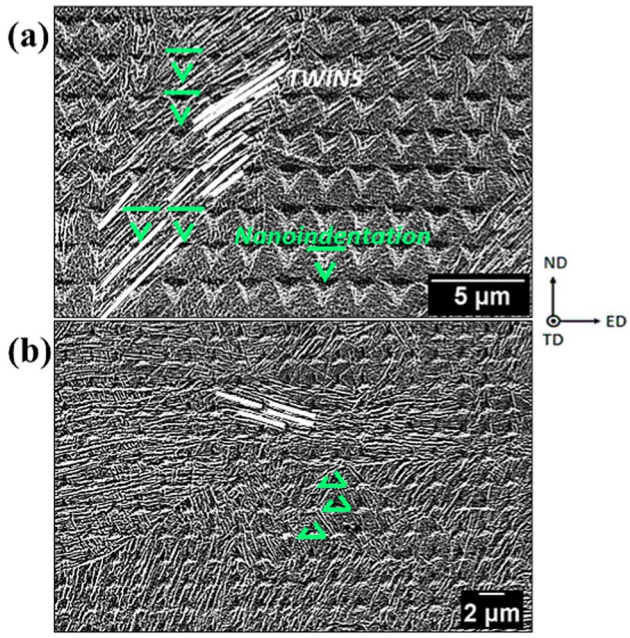

Fig. 13 FEG-SEM secondary electron micrographs of samples, showing the microstructure evolution from (**a**) after 1 ECAP pass and (**b**) after 4 ECAP passes. Mechanical twins are highlighted with white arrows, while nanoindentation prints are marked in green

with a higher number of twins from deformation bands and grain boundary zones, but an increase of the hardness and elastic modulus is observed related with the increase of twins (harder). This is due to the fact that the microstructure is completely disorganized and work-hardened. Despite clear qualitative trends, the nanohardness and elastic modulus values presented in Table 2 were calculated as mean values of the measurements. The results are consistent with that presented by previous published research [65].

From the obtained maps of H, one can see that, as expected for the investigated steel, it is more difficult to deform the material as the number of ECAP pass increases. This may be due to the low stacking fault energy (SFE) of the material, which in turn promotes multiplication and more uniform distribution of dislocation. From the elastic modulus analysis, the material after ECAP passes had a high (E) value, evidencing the material's capacity to resist tensions, without deformation or rupture. Conversely, the disparity in properties is more distinct in the H/E ratio map. While H and E signify distinct mechanical behaviors, their values are interconnected in a manner where the resulting H/E ratio consistently exhibits uniform values. The results are consistent with those presented in a previous publication [39].

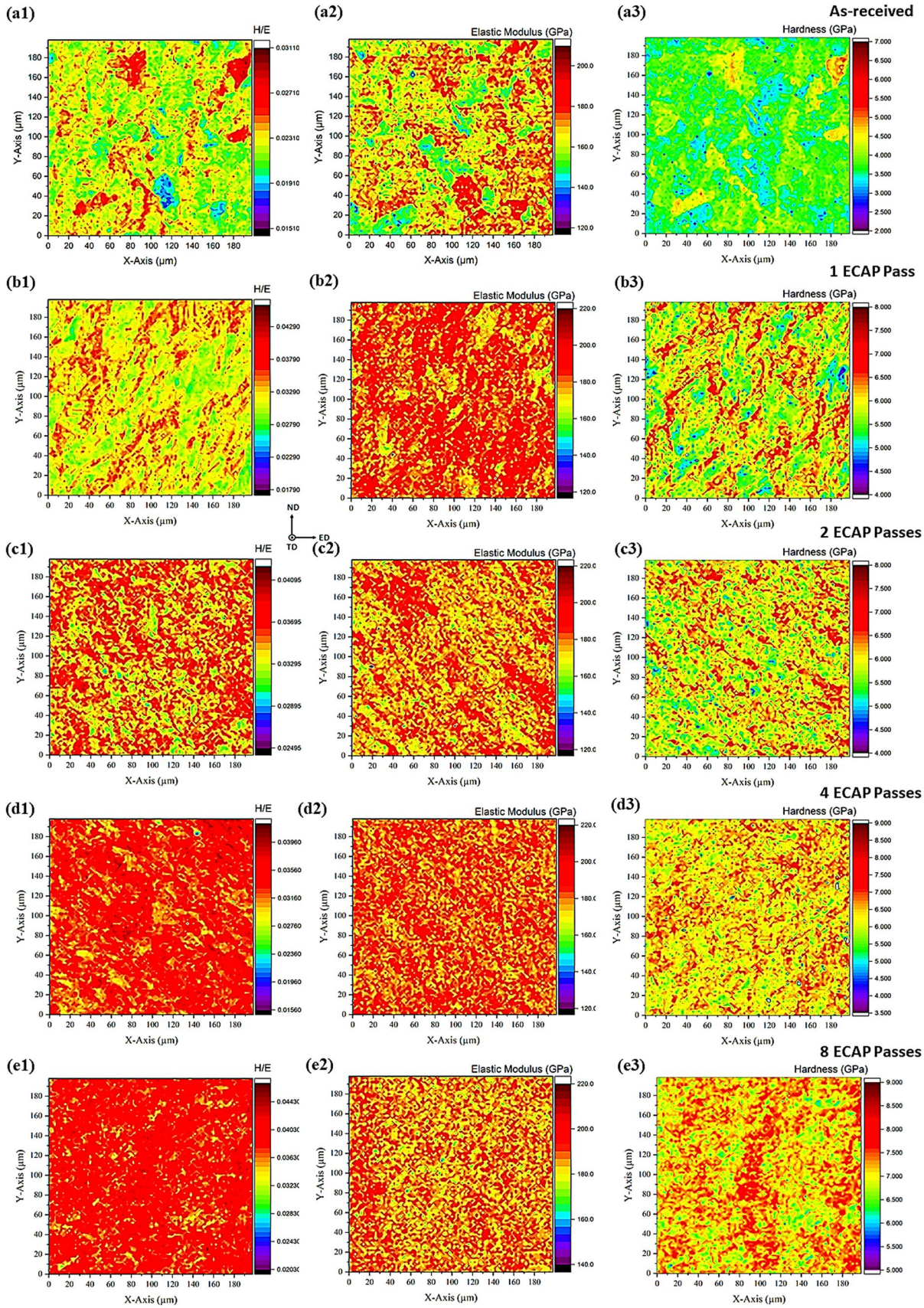
(a1)
H/E
(a2)
Elastic Modulus (GPa)
(a3)
As-received
Hardness (GPa)
(b1)
H/E
(b2)
Elastic Modulus (GPa)
(b3)
1 ECAP Pass
Hardness (GPa)
ND
TD
ED
(c1)
H/E
(c2)
Elastic Modulus (GPa)
(c3)
2 ECAP Passes
Hardness (GPa)
(d1)
H/E
(d2)
Elastic Modulus (GPa)
(d3)
4 ECAP Passes
Hardness (GPa)
(e1)
H/E
(e2)
Elastic Modulus (GPa)
(e3)
8 ECAP Passes
Hardness (GPa)
X-Axis (μm)
Y-Axis (μm)

◂**Fig. 14** Hardness and Elastic modulus nanoindentation maps of the analyzed TWIP steel for (**a1**, **a2**, **a3**) as-received, (**b1**, **b2**, **b3**) post 1 ECAP pass, (**c1**, **c2**, **c3**) post 2 ECAP passes, (**d1**, **d2**, **d3**) post 4 ECAP passes, and (**e1**, **e2**, **e3**) post 8 ECAP passes

3.5 Micromechanical Characterization Behavior

Figure 15 and Table 3 present the microtensile test outcomes for the as-received TWIP steel samples and those processed by ECAP. This research shows that the number of ECAP passes contributed to the increase of yield strength (YS) and ultimate tensile strength (UTS). It is noticeable that the increase in yield strength is more pronounced than the corresponding increase in ultimate tensile strength. This trend has also been observed in previous studies [22, 66–68]. The occurrence of serrated flow in the as-received sample, visible as notches on the tensile test curve, arises from dynamic aging prompted by stress-induced interactions between C-Mn clusters and partial dislocations [33, 68]. Despite a reduction in total elongation and ductility with each ECAP pass, the obtained values for elongation and toughness can still be considered satisfactory. The elongation values noted in this study surpass those documented for certain conventional deep drawing steels like high strength interstitial-free (HS-IF) steel and other high manganese TWIP steels [66, 69].

Yield strength undergoes a significant increase after the first pass of equal channel angular pressing (ECAP) at 350°C in the FeMnCCr-based TWIP steel. This is due to increased dislocation movement activity, which leads to the formation of many subgrains and interactions with mechanical twinning [70]. Similar observations were reported in earlier investigations on severe plastic deformation (SPD) using ECAP at comparable temperatures for FeMnC-based TWIP steels [17] and FeMnCAl-based TWIP steels [28]. There are no documented instances in literature of severe plastic deformation (SPD) being conducted on TWIP steels that are based on FeMnCCr. Despite the increase in SFE values at 350 °C reported in previous studies [27, 71], mechanical twinning persisted within the austenite grains of the present TWIP steel, as well as in other TWIP steels subjected to ECAP processing, as detailed in earlier literature [17]. Haase et al. [22] reported that the FeMnCAl TWIP steel deformed at 300 °C also exhibited uniform elongation values similar to the steel studied in this work. The satisfactory elongation and toughness of the current TWIP steel after ECAP can be attributed to several factors [72]. The initial microstructure of the steel and the microstructure after one ECAP pass may be contributing to this behavior. The deformation mechanisms involved in the steel's tensile tests at room temperature also contribute to its elongation and toughness.

The as-received sample exhibits high plasticity due to the large number of slip systems and free path for dislocations to move within the austenitic matrix. The increase in dislocation density during the deformation process promotes the TWIP effect, which is observed during the micro tensile test at room temperature. When many subgrains are formed, the movement of dislocations is restricted, which causes the steel to start deforming by secondary sliding systems. There is the dissociation of dislocations into partial Schockley dislocations. This observation is consistent with the findings of Barbier et al. [73] who investigated the microstructural changes of a FeMnC TWIP steel under tensile and shear tests. The proportion of twinned grains was found to be lower in the steel sample after undergoing the shear test, with only 70% of grains exhibiting active twinning compared to 90% in the sample tested under tensile conditions. In this case, the microstructure exhibits a significant number of elongated grains that contain a high density of mechanical twins and subgrains. Additionally, there are some regions in the microstructure that contain fewer defects. The combined microstructure supports the retention of acceptable elongation. Chromium is a potent alloying component in steel, and it is found in small quantities in specific structural steels. The primary application of chromium is to enhance the hardenability and corrosion resistance of steel and to boost its yield strength. The addition of chromium to steel lowers the stacking fault energy, which promotes the TWIP effect [26, 74–76].

The TWIP steel used here has a low SFE, which promotes twinning. During tensile deformation, the activation of secondary twins is favored at extremely low deformations [73]. The combination of two factors, namely, minimal grain deformation and enhanced susceptibility to twinning during tensile testing at room temperature, may account for the substantial elongation observed in the samples subjected to a single pass of ECAP. It is possible to suggest that the primary deformation mechanism was mechanical twinning, as described in previous studies [19, 24]. The TWIP steel investigated showed a high work hardening capacity, as mechanical twins were detected even after 4 ECAP passes [40], indicating that mechanical twinning was still an active deformation mechanism. This can be seen in Fig. 8 where low angles boundary increases after 1 and 2 ECAP passes. Also, Fig. 14 shows the increase of the microhardness, indicating the work hardening mechanism.

The behavior observed after 2 ECAP passes at 350°C is similar to that observed at room temperature: an increase in resistance and a decrease in total elongation. The two phenomena could be associated with the development of the microstructure. The analysis of the EBSD presented in Figs. 6 and 7 illustrates a remarkable decrease in the dimensions of grains and subgrains as a result of the accumulated strain. It is worth mentioning that a previous study on a similar TWIP steel after 2 ECAP passes reported the presence of nano-twins within the primary twins as a result of secondary

Table 2 The nanoindentation values of the maps of the examined TWIP steel used to derive parameters such as the elastic modulus (E) and nanohardness (H)

ECAP schedules	As-received	1 pass	2 passes	4 passes	8 passes
H (GPa)	3.76 ± 0.4	5.91 ± 0.5	5.98 ± 0.3	6.40 ± 0.3	7.38 ± 0.4
E (GPa)	166.56 ± 3.4	178.54 ± 2.7	182.08 ± 4.2	183.03 ± 4.1	186.80 ± 3.5

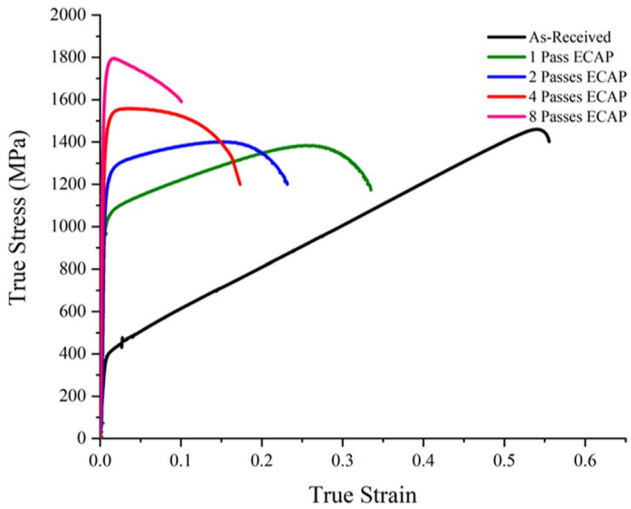

Fig. 15 Stress/logarithmic strain curves of the investigated samples

twinning [19, 24]. Mechanical twins significantly reduce the mean free path of dislocations, resulting in a drastic increase in mechanical strength. Compared to similar steels processed by ECAP, the steel being studied exhibits higher yield strength (YS) values, ultimate tensile strength (UTS), toughness, elongation, and resilience.

The maximum strength of 1.8 GPa was observed in the TWIP steel after 8 ECAP passes, but elongation was significantly reduced. Here, the mechanical properties were higher than in previous research with different materials for riser applications [77, 78]. The elongation value after 4 passes is also acceptable for this application as reported elsewhere [77–80]. The microstructure refinement observed in the EBSD and SEM analysis corresponds well with the increase in strength and decreased elongation observed after 8 ECAP passes in the TWIP steel. New refined grains with an equiaxed morphology were formed due to the subgrains formed in previous ECAP passes. The image in Fig. 4 illustrates that the dislocation density increased slowly between the fourth and eighth passes. Upon analysis of the EBSD, KAM and texture intensity values, it can be inferred that the TWIP steel likely underwent a recrystallization process, forming new ultrafine grains. After each pass, there was a significant increase in resilience values, but toughness and elongation decreased. Each pass of ECAP caused a distortion in the crystalline network of the TWIP austenitic steel, as confirmed by the XRD analysis shown in Fig. 4 [81, 82].

Fracture surface examination was conducted and is illustrated in Fig. 16. The surface characteristics of the initial specimen showed numerous dimples that varied in size and depth. The images obtained are consistent with the reported elongation and toughness results; see Table 3. The fracture surface of the annealed material appears ductile, whereas for the samples after 4 and 8 passes of ECAP, the surface changes to show tiny voids without coalescence, indicating a brittle material surface. According to some researchers [83], a material's plastic deformation capacity improves with larger and deeper dimples, leading to increased elongation during tensile testing. Figure 16b shows that the sample after 1 ECAP pass exhibits a ductility level that is intermediate between the highly ductile as-received sample (Fig. 16a) and the limited ductility of the sample after 4 ECAP passes (Fig. 16d). The cleavage on samples processed by ECAP implies that ductility mechanisms are still active, although the material underwent strain hardening during processing. Although microstructural refinement limits dislocation movement, it seems that the twinning mechanism still contributes to toughness, as indicated by the small size of voids and ripples in the samples following ECAP processing, mainly after 2 and 4 passes. The effect of mechanical twinning

Table 3 The mechanical behavior of the investigated TWIP steel analyzed under various conditions using true stress-true strain curves to define its mechanical properties

ECAP schedules	Yield strength (MPa)	Ultimate tensile strength (MPa)	Resilience (MJ m^{-3})	Elongation (%)	Toughness (MJ m^{-3})
As-received	377 ± 2	1460 ± 5	1.71	57 ± 5	593.81
1 pass	1035 ± 5	1385 ± 3	6.88	34 ± 2	421.20
2 passes	1210 ± 3	1402 ± 2	7.46	23 ± 1	307.00
4 passes	1495 ± 2	1560 ± 2	10.25	17 ± 2	243.70
8 passes	1727 ± 3	1800 ± 3	11.18	10 ± 1	173.12

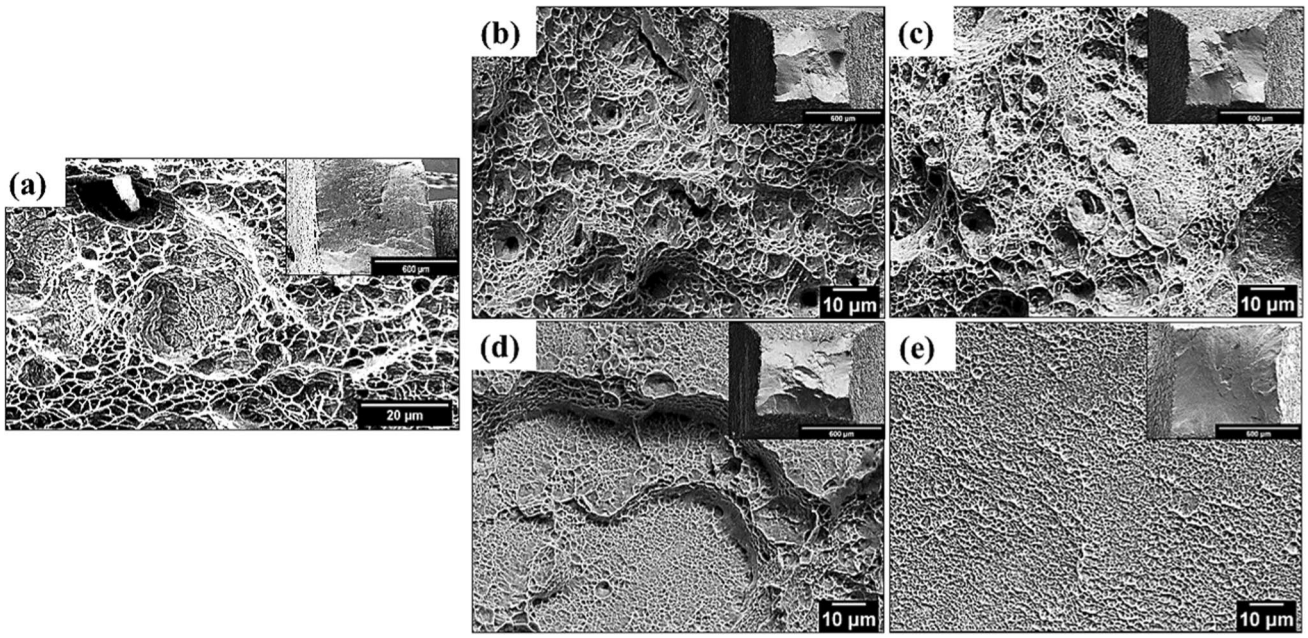

Fig. 16 Fracture surfaces of five different samples after tensile testing: (**a**) the as-received sample, (**b**) the sample after 1 ECAP pass, (**c**) the sample after 2 ECAP passes, (**d**) the sample after 4 ECAP passes, and (**e**) the sample after 8 ECAP passes

may be attributed to the tensile test temperature (room temperature), according to this observation. Based on the dimples observed on the fracture surface of samples with 8 ECAP passes (Fig. 16e), it can be inferred that the material retains some level of strain hardening [84].

Yanagimoto et al. [85] have distinguished between two types of dimples associated with ductile fracture. The larger dimples arise from the decohesive mechanism within the inclusion-matrix interphase, while the smaller dimples stem from the dislocation interaction mechanism [48]. Upon ECAP, there is a refinement and diversification in the dimple size. Notably, the fracture surface of ECAP-ed samples displays a greater prevalence of small dimples in comparison to the annealed specimens. This discrepancy is ascribed to a substantial increase in dislocation density following a singular ECAP pass, making it easier for dislocations to reach the grain boundary. Consequently, the transformation of dislocations into multiple unstable crack initiations, forming the nucleus of cavities, becomes more feasible.

4 Conclusions

TWIP steel containing Chromium was successfully subjected to isothermal equal channel angular pressing. The microstructure changes, texture, and mechanical performance of the material were examined. The main results obtained were:

(1) After one or two ECAP passes, the microstructure evolved by elongating the grains in the shear direction and introducing a considerable amount of subgrains. Simultaneously, the mechanical twinning occurred with decreasing thickness as the deformation progressed. The microstructure refinement continued during the ECAP passes due to the activity of dislocations and twinning, causing hindrance in further deformation. This resulted in a low hardening rate for the eight ECAP passes sample during the tensile test.

(2) Simple shear textures were observed in the material after undergoing deformation through ECAP. Samples after one ECAP pass exhibited a preference for A1*, A2*, and C components, whereas the two and four ECAP pass samples showed a preference for the B fiber, as indicated by its $B/\overline{B}$ components. The increase in $B/\overline{B}$ components, along with the decrease in C shear texture component, may suggest a significant impact of deformation twinning during the processing of TWIP steel by ECAP at the tested temperature.

(3) The hardness and elastic modulus maps demonstrated a notable connection between micromechanical properties and the strain imposed by simple shear. The precision and clarity of this relationship were enhanced through the utilization of H/E maps. Consequently, the H/E ratio is suggested as a suitable and dependable parameter. The ECAP process produced higher hardness and modulus values than the as-received material. It is possible that the evaluated changes related to the

small-scale properties are related to work hardening effects, crystalline defects (twins and shear bands), and the material's texture. Finally, the nanoindentation maps indicated that the ECAP-processed samples exhibited isotropic mechanical characteristics, showcasing the impact of grain refinement on both nano and micromechanical behavior of the material.

(4) The ECAP process resulted in a notable increase in both the yield strength and ultimate tensile strength. However, as the number of passes increased, the ductility and toughness of the material decreased. As the number of ECAP passes increased, the fracture surface analysis revealed a significant reduction in the number and size of dimples. The eight ECAP passes sample displayed limited ductile fracture. These behaviors are attributed to the metal's ability to deform via twinning, wherein primary and secondary twin systems are activated. The strain hardening rate decreased gradually with increasing strain, leading to uniform elongation.

(5) As the degree of deformation increased, the material underwent a gradual development of shear bands and a corresponding increase in dislocation density. This in turn facilitated dislocation glide and the activation of twin-induced plasticity, resulting in a favorable balance between strength and elongation.

Acknowledgements This work has been supported by the following Brazilian research agencies: Cearense Foundation to Support Scientific and Technological Development-FUNCAP; Coordenação de Aperfeiçoamento de Pessoal de Nível Superior—Brasil (CAPES)—Finance Code 001 CAPES; Research and Support Foundation of Maranhão (FAPEMA); Brazilian National Council for Scientific and Technological Development (CNPq). The authors also acknowledge with gratitude the Materials Characterization Laboratory (LACAM) and Analytical Central from Federal University of Ceará (UFC).

Author Contributions Not applicable.

Data Availability The datasets generated during and/or analyzed during the current study are available from the corresponding authors on reasonable request.

Declarations

Conflict of interest The authors declare that they have no conflict of interest or competing interests.

Ethical Approval The authors have adhered to the accepted ethical standards of a genuine research study.

References

1. Y.Z. Li, Z.Y. Liang, M.X. Huang, Int. J. Plast. **150**, 103198 (2022)
2. G. Frommeyer, U. Brüx, P. Neumann, ISIJ Int. **43**, 438 (2003)
3. O. Grässel, L. Krüger, G. Frommeyer, L.W. Meyer, Int. J. Plast. **16**, 1391 (2000)
4. W.S. Choi, S. Sandlöbes, N.V. Malyar, C. Kirchlechner, S. Korte-Kerzel, G. Dehm, B.C. De Cooman, D. Raabe, Acta Mater. **132**, 162 (2017)
5. O. Bouaziz, S. Allain, C.P. Scott, P. Cugy, D. Barbier, Curr. Opin. Solid State Mater. Sci. **15**, 141 (2011)
6. K.M. Rahman, V.A. Vorontsov, D. Dye, Acta Mater. **89**, 247 (2015)
7. M.J. Sohrabi, H. Mirzadeh, S. Sadeghpour, R. Mahmudi, Int. J. Plast. **160**, 103502 (2023)
8. H. Zhi, C. Zhang, S. Antonov, H. Yu, T. Guo, Y. Su, Acta Mater. **195**, 371 (2020)
9. Z.G. Liu, X.H. Gao, M. Xiong, P. Li, R.D.K. Misra, D.Y. Rao, Y.C. Wang, Mater. Sci. Eng. A **807**, 140881 (2021)
10. R. Valiev, Nat. Mater. **3**, 511 (2004)
11. C.S. Meredith, A.S. Khan, Int. J. Plast. **30–31**, 202 (2012)
12. K.-H. Jung, D.-K. Kim, Y.-T. Im, Y.-S. Lee, Int. J. Plast. **42**, 120 (2013)
13. P. Wang, Y. Xiang, X. Wang, Z. Liu, S. Qu, Z. Zhuang, Int. J. Plast. **123**, 22 (2019)
14. M.F.-X. Wagner, N. Nostitz, S. Frint, P. Frint, J. Ihlemann, Int. J. Plast. **134**, 102755 (2020)
15. A.S. Khan, C.S. Meredith, Int. J. Plast. **26**, 189 (2010)
16. M.M. Abramova, N.A. Enikeev, J.G. Kim, R.Z. Valiev, M.V. Karavaeva, H.S. Kim, Mater. Lett. **166**, 321 (2016)
17. I.B. Timokhina, A. Medvedev, R. Lapovok, Mater. Sci. Eng. A **593**, 163 (2014)
18. M. Shirani, N. Anjabin, H.S. Kim, Mater. Sci. Technol. **37**, 1291 (2021)
19. L. Wang, J.A. Benito, J. Calvo, J.M. Cabrera, J. Mater. Eng. Perform. **26**, 554 (2017)
20. E. Bagherpour, M. Reihanian, R. Ebrahimi, Mater. Des. **36**, 391 (2012)
21. R.Z. Valiev, A.P. Zhilyaev, T.G. Langdon, *Bulk Nanostructured Materials* (Wiley, Hoboken, 2013)
22. C. Haase, O. Kremer, W. Hu, T. Ingendahl, R. Lapovok, D.A. Molodov, Acta Mater. **107**, 239 (2016)
23. M. Abramova, A. Raab, R.Z. Valiev, A. Khannanova, C.S. Lee, J.N. Kim, G.H. Jang, J.G. Kim, H.S. Kim, O. Renk, N. Enikeev, Metals **11**, 518 (2021)
24. L. Wang, J.A. Benito, J. Calvo, J.M. Cabrera, J. Mater. Sci. **52**, 6291 (2017)
25. G. Yang, J.-K. Kim, Metals **11**, 124 (2021)
26. S. Lee, J. Kim, S.-J. Lee, B.C. De Cooman, Scr. Mater. **65**, 1073 (2011)
27. S. Allain, J.-P. Chateau, O. Bouaziz, S. Migot, N. Guelton, Mater. Sci. Eng. A **387–389**, 158 (2004)
28. A. Dumay, J.-P. Chateau, S. Allain, S. Migot, O. Bouaziz, Mater. Sci. Eng. A **483–484**, 184 (2008)
29. C.-Y. Chou, S.-L. Lee, J.-C. Lin, Mater. Chem. Phys. **107**, 193 (2008)
30. E. Damavandi, S. Nourouzi, S.M. Rabiee, R. Jamaati, J.A. Szpunar, Met. Mater. Int. **27**, 2756 (2021)
31. G.I. Raab, I.S. Kodirov, D.A. Aksenov, R.Z. Valiev, J. Alloys Compd. **922**, 166205 (2022)
32. Y. Iwahashi, Z. Horita, M. Nemoto, T.G. Langdon, Acta Mater. **46**, 3317 (1998)
33. M.N.S. Lima, R.C.P. Loureiro, M. Béreš, M. Masoumi, J.C. Muñoz, S.F. Rodrigues, H.F. Gomes-de-Abreu, J.M. Cabrera-Marrero, J. Mater. Res. Technol. **19**, 7 (2022)
34. W. Pantleon, Scr. Mater. **58**, 994 (2008)
35. B. Beausir, J.-J. Fundenberger, Analysis Tools for Electron and X-ray diffraction (ATEX - software, Université de Lorraine-Metz, 2017), https://www.atex-software.eu/
36. W.C. Oliver, G.M. Pharr, J. Mater. Res. **7**, 1564 (1992)
37. W.C. Oliver, G.M. Pharr, J. Mater. Res. **19**, 3 (2004)

38. P. Sudharshan-Phani, W.C. Oliver, Mater. Des. **164**, 107563 (2019)
39. H. Besharatloo, M. Carpio, J.-M. Cabrera, A.M. Mateo, G. Fargas, J.M. Wheeler, J.J. Roa, L. Llanes, Metals **10**, 1352 (2020)
40. M.N. da Silva-Lima, S.F. Rodrigues, M. Al-Maharbi, J.C. Muñoz, J.M. Cabrera-Marrero, H.F. Gomes de Abreu, J. Mater. Res. Technol. **24**, 1757 (2023)
41. M.N. da Silva Lima, G.L. França Schmalz, R.C.P. Loureiro, J.C. Ferreira, S.F. Rodrigues, J.C. Muñoz, J.M.C. Marrero, H.F.G. de Abreu, Mater. Sci. Eng. A **877**, 145206 (2023)
42. F. Ye, T. Zhu, K. Mori, Q. Xu, Y. Song, Q. Wang, R. Yu, B. Wang, X. Cao, J. Alloys Compd. **876**, 160134 (2021)
43. J.G.M. van Berkum, R. Delhez, Th.H. de Keijser, E.J. Mittemeijer, Acta Crystallogr. A **52**, 730 (1996)
44. T. Ungár, Scr. Mater. **51**, 777 (2004)
45. A.D. Prasetya, M. Rifai, A. Mujamilah, H. Miyamoto, J. Phys. Conf. Ser. **1436**, 012113 (2020)
46. O. Zinovieva, A. Zinoviev, V. Romanova, R. Balokhonov, Addit. Manuf. **36**, 101521 (2020)
47. N. Zhang, P. Yang, W. Mao, Mater Charact **119**, 225 (2016)
48. O.F. Higuera-Cobos, J.M. Cabrera, Mater. Sci. Eng. A **571**, 103 (2013)
49. A. Després, M. Zecevic, R.A. Lebensohn, J.D. Mithieux, F. Chassagne, C.W. Sinclair, Acta Mater. **182**, 184 (2020)
50. É.F. Prados, V.L. Sordi, M. Ferrante, Mater. Res. **11**, 199 (2008)
51. I.J. Beyerlein, L.S. Tóth, Prog. Mater. Sci. **54**, 427 (2009)
52. O.F. Higuera-Cobos, J.A. Berríos-Ortiz, J.M. Cabrera, Mater. Sci. Eng. A **609**, 273 (2014)
53. I.J. Beyerlein, L.S. Tóth, C.N. Tomé, S. Suwas, Phil. Mag. **87**, 885 (2007)
54. A. Saeed-Akbari, L. Mosecker, A. Schwedt, W. Bleck, Metall. and Mater. Trans. A. **43**, 1688 (2012)
55. S.G. Chowdhury, J. Gubicza, B. Mahato, N.Q. Chinh, Z. Hegedűs, T.G. Langdon, Scr. Mater. **64**, 1007 (2011)
56. X. Molodova, R. Berghammer, G. Gottstein, R.J. Hellmig, Int. J. Mater. Res. **98**, 158 (2007)
57. A.A. Gazder, F.D. Torre, C.F. Gu, C.H.J. Davies, E.V. Pereloma, Mater. Sci. Eng. A **415**, 126 (2006)
58. S. Li, I.J. Beyerlein, D.J. Alexander, S.C. Vogel, Scr. Mater. **52**, 1099 (2005)
59. X. Molodova, G. Gottstein, M. Winning, R.J. Hellmig, Mater. Sci. Eng. A **460–461**, 204 (2007)
60. S. Suwas, L.S. Tóth, J.J. Fundenberger, A. Eberhardt, W. Skrotzki, Scr. Mater. **49**, 1203 (2003)
61. H. Idrissi, K. Renard, L. Ryelandt, D. Schryvers, P.J. Jacques, Acta Mater. **58**, 2464 (2010)
62. N.P. Gurao, P. Kumar, B. Bhattacharya, A. Haldar, S. Suwas, Metall. Mater. Trans. A **43**, 5193 (2012)
63. S.I. Wright, M.M. Nowell, D.P. Field, Microsc. Microanal. **17**, 316 (2011)
64. K. Li, P. Yang, Metals **7**, 412 (2017)
65. G.M. Claudia, G. Ivan, O.M. Laia, J.P. Emilio, G. Maria-Pau, V. Maurizio, C. José-Luís, P. Marta, Mater. Des. **228**, 111817 (2023)
66. K. Hajizadeh, B. Eghbali, K. Topolski, K.J. Kurzydlowski, Mater. Chem. Phys. **143**, 1032 (2014)
67. M. Shaban-Ghazani, H. Irani, S.H. Mohitfar, Mater. Chem. Phys. **271**, 124952 (2021)
68. M.C. Jo, M.C. Jo, A. Zargaran, S.S. Sohn, N.J. Kim, S. Lee, Mater. Sci. Eng. A **806**, 140823 (2021)
69. G. Frommeyer, E.J. Drewes, B. Engl, Revue de Métallurgie **97**, 1245 (2000)
70. L. Bracke, K. Verbeken, L. Kestens, J. Penning, Acta Mater. **57**, 1512 (2009)
71. O. Bouaziz, N. Guelton, Mater. Sci. Eng. A **319–321**, 246 (2001)
72. M. Dehghan, R. Miresmaeili, M. Askari-Paykani, H.R. Shahverdi, Met. Mater. Int. **28**, 1232 (2022)
73. D. Barbier, V. Favier, B. Bolle, Mater. Sci. Eng. A **540**, 212 (2012)
74. S.G. Lee, B. Kim, M.C. Jo, K.-M. Kim, J. Lee, J. Bae, B.-J. Lee, S.S. Sohn, S. Lee, J. Mater. Sci. Technol. **50**, 21 (2020)
75. M. Cheng, P. He, L. Lei, X. Tan, X. Wang, Y. Sun, J. Li, Y. Jiang, Corros. Sci. **183**, 109338 (2021)
76. N. Guo, C. Sun, M. Fu, M. Han, Metals **7**, 348 (2017)
77. M. Masoumi, M.A. Mohtadi Bonab, J.L. Cardoso, L. Novotný, R.C.P. Loureiro, P.H. Pinheiro, M. Béreš, H.F.G. de Abreu, J. Mater. Res. Technol. **26**, 9406 (2023)
78. P.B.P. Leão, S. Zhang, J.R.B. Neto, S.A. Freire, R.C.P. Loureiro, A.J. Ramirez, H.F.G. de Abreu, J. Mater. Process. Technol. **316**, 117950 (2023)
79. P.B. Paiva Leão, J.R. Barros Neto, S.F. Rodrigues, L. Novotný, J.L. Cardoso, L.F.G. Herculano, T.N. Lima, A.J. Ramirez, H.F.G. de Abreu, J. Mater. Res. Technol. **24**, 9441 (2023)
80. P.H. Pinheiro-Lima, S.K. Bezerra de Lima, M.V. Goncalves Rodrigues, L.F. Gaspar Herculano, R.C. de Paes Loureiro, S.A. Freire, J.L. Cardoso, M. Masoumi, G.S. Reis, E.S. Silva, S.F. Rodrigues, H.F. Gomes de Abreu, J. Mater. Res. Technol. **26**, 1984 (2023)
81. K. Renard, P.J. Jacques, Mater. Sci. Eng. A **542**, 8 (2012)
82. J.-E. Jin, Y.-K. Lee, Acta Mater. **60**, 1680 (2012)
83. J. Ren, Q. Chen, J. Chen, Z. Liu, Mater. Sci. Eng. A **811**, 141063 (2021)
84. M. Etemadi, A.M. Rashidi, A. Zajkani, Met. Mater. Int. **28**, 1075 (2022)
85. J. Yanagimoto, J. Tokutomi, K. Hanazaki, N. Tsuji, CIRP Ann. **60**, 279 (2011)

Publisher's Note Springer Nature remains neutral with regard to jurisdictional claims in published maps and institutional affiliations.

Springer Nature or its licensor (e.g. a society or other partner) holds exclusive rights to this article under a publishing agreement with the author(s) or other rightsholder(s); author self-archiving of the accepted manuscript version of this article is solely governed by the terms of such publishing agreement and applicable law.

Authors and Affiliations

Marcos Natan da Silva Lima[1,2,6] · Samuel Filgueiras Rodrigues[3] · Majid Al-Maharbi[4] · Laia Ortiz-Membrado[5] · Maria Veronica Goncalves Rodrigues[3] · Jessica Calvo Muñoz[6] · Emilio Jiménez-Piqué[5] · Gedeon Silva Reis[3] · José María Cabrera Marrero[6] · Hamilton Ferreira Gomes de Abreu[1,2]

✉ Samuel Filgueiras Rodrigues
samuel.filgueiras@ifma.edu.br

[1] Materials Characterization Laboratory (LACAM), Department of Metallurgical and Materials Engineering, Federal University of Ceará, Campus do Pici, Bloco 729, Fortaleza, Ceará 60020-181, Brazil

[2] Graduate Program in Materials Science and Engineering, Department of Metallurgical and Materials Engineering,

Universidade Federal do Ceará, Campus do Pici, Building 729, Fortaleza 60.440-554, Brazil

[3] Graduate Program in Materials Engineering, Federal Institute of Education, Science and Technology of Maranhão, Sao Luis, Maranhão 65030-005, Brazil

[4] Department of Mechanical and Industrial Engineering, Sultan Qaboos University, Muscat, Oman

[5] Structural Integrity, Micromechanics and Reliability of Materials Group, Department of Materials Scien Bcce and Engineering, UPC, EEBE, 08019 Barcelona, Spain

[6] Processes for Conformation of Metallic Materials (PROCOMAME), Department Materials Science and Metallurgical Engineering, Universitat Politècnica de Catalunya, 08930 Barcelona, Catalonia, Spain